Behavior of New Zealand Ironsand During Iron Ore Sintering

ZHE WANG, DAVID PINSON, SHENG CHEW, HAROLD ROGERS, BRIAN J. MONAGHAN, MARK I. POWNCEBY, NATHAN A.S. WEBSTER, and GUANGQING ZHANG

A New Zealand ironsand sample was characterized by scanning electron microscopy (SEM), X-ray fluorescence spectroscopy, qualitative and quantitative X-ray diffraction, and electron probe microanalysis. The titanomagnetite-rich ironsand was added into an industrial sinter blend in the proportion of 5 wt pct, and the mixture was uniaxially pressed into cylindrical tablets and sintered in a tube furnace under flowing gas with various oxygen potentials and temperatures to develop knowledge and understanding of the behavior of titanium during sintering. An industrial sinter with the addition of 3 wt pct ironsand was also examined. Both the laboratory and industrial sinters were characterized by optical and SEM. Various morphologies of relict ironsand particles were present in the industrial sinter due to the heterogeneity of sintering conditions, which could be well simulated by the bench-scale sintering experiments. The assimilation of ironsand during sintering in a reducing atmosphere started with the diffusion of calcium into the lattice of the ironsand matrix, and a reaction zone was formed near the boundary within individual ironsand particles where a perovskite phase was generated. With increasing sintering temperature, in a reducing atmosphere, ironsand particles underwent further assimilation and most of the titanium moved from the ironsand particles into a glass phase. In comparison, more titanium remained in the original ironsand particles when sintered in air. Ironsand particles are more resistant to assimilation in an oxidizing atmosphere.

I. INTRODUCTION

IRONSAND deposits along the western coast of the North Island of New Zealand are currently mined as iron ores for steel production.[1] The composition of the New Zealand ironsands approximates that of titanomagnetite ($Fe_{3-x}Ti_xO_4$) containing about 60 wt pct iron, 8 wt pct titania (TiO_2), and a small amount of other impurities such as silica, phosphorus, and lime.[1–3] Recently, BlueScope's Port Kembla sinter plant has begun incorporating 2 to 3 wt pct ironsand as a component of its iron ore sinter blend. The ironsand provides a cheaper, alternative source of iron, and its incorporation into sinter provides an appropriate method of its utilization in ironmaking as its small particle size precludes direct charging into a blast furnace.[4] The introduction of a minor amount of titanium-bearing burden into blast furnaces has previously been demonstrated to be beneficial through the formation of titanium carbonitride precipitates that can deposit on the hearth lining and, consequently, extend operating campaigns.[5,6]

Limited work[4,7,8] on the addition of titanium-bearing minerals *via* a sinter plant indicates that a high level of Ti in the sinter mix may reduce productivity, lower sinter strength, and result in deterioration of sinter reducibility. In the most comprehensive study, Bristow and Loo[4] examined the effect of addition of an ironsand from New Zealand into two iron ore blends containing 10 and 20 pct pisolitic limonite, respectively, on the properties of sinter prepared using a pilot-scale sintering facility. It was found that the addition of up to 2 pct titanomagnetite did not significantly affect the sinter quality; however, increasing the titanomagnetite levels to greater than 3 pct caused a significant increase in the reduction degradation index (RDI) of the sinters. It was postulated that the addition of titanium decreased the fracture toughness of glass phase which is the weakest phase in a sinter and would increase the vulnerability of the sinter to crack propagation, thereby resulting in deterioration in sinter RDI.

While the previous studies have provided useful information on how the addition of titanomagnetite potentially affects sinter quality, no satisfactory conclusion has been forthcoming as to how the titanomagnetite

ZHE WANG, Ph.D. Student, HAROLD ROGERS, Senior Research Fellow, BRIAN J. MONAGHAN, Professor, and GUANGQING ZHANG, Lecturer, are with the School of Mechanical, Materials & Mechatronic Engineering, University of Wollongong, Wollongong, NSW 2522, Australia. Contact e-mail: gzhang@uow.edu.au. DAVID PINSON, Senior Research Engineer, and SHENG CHEW, Principal Research Engineer, are with the Steelmaking Technology and Planning, BlueScope, PO Box 202, Port Kembla, NSW 2505, Australia. MARK I. POWNCEBY, Principal Research Scientist, and NATHAN A. S. WEBSTER, Research Scientist, are with CSIRO Mineral Resources Flagship, Private Bag 10, Clayton South, VIC 3169, Australia.

changes or reacts during the sintering process. The lack of information is largely due to the complexity of the raw materials involved and their mutual interactions during sintering. In this study, a detailed characterization of an ironsand concentrate was conducted, and the behavior of the ironsand during sintering was investigated to gain a better understanding of the sintering mechanism of titanomagnetite. An industrially prepared sinter with the addition of 3 wt pct of ironsand was also characterized as part of the study to compare the behavior of titanium during sintering derived from the appearance of the ironsand relics.

II. EXPERIMENTAL PROCEDURE

Bench-scale sintering tests using iron ore mixes containing 5 wt pct ironsand were carried out. The sintered samples were characterized by optical microscopy and scanning electron microscopy with energy-dispersive X-ray spectroscopy (SEM/EDS) analyses.

A. Raw Materials and Preparation

The starting materials for the bench-scale iron ore sintering experiments were a bulk iron ore blend, limestone, dolomite, silica sand, manganese ore, cold return fines (CRF), and ironsand from New Zealand. The iron ore blend contained hematite and goethite ores produced in Western Australia. All components were supplied by BlueScope Ltd. The major chemical compositions of the raw materials are listed in Table I. Each raw material component (except the ironsand) was crushed and screened to less than 200 μm. This was to make sure that the sample composition and sintering conditions were uniform when sintered in a small tablet. These materials were then mixed in the proportion corresponding to that of BlueScope's bulk sinter blend before the ironsand was added and mixed thoroughly to ensure homogeneity. The final raw material mixture contained iron ore blend 61.7 wt pct, limestone 9.7 wt pct, dolomite 1.8 wt pct, silica sand 0.1 wt pct, CRF 21.7 wt pct, and ironsand 5.0 wt pct. The overall basicity (CaO/SiO$_2$ mass ratio) of the mixture was 2.0. The final sinter blend was pressed into cylindrical tablets of 5 mm diameter and ~5 mm height for the sintering experiments. Each tablet weighed ~0.3 g.

B. Bench-scale Sintering

A schematic of the sintering apparatus is shown in Figure 1. The setup utilizes a vertical tube furnace with a working tube of 55 mm internal diameter through which a gas mixture of controlled composition is continuously passed. A type R thermocouple was inserted from furnace bottom with its tip located below the sample crucible to monitor the sintering temperature. Experiments were conducted at a range of temperatures (1523 K, 1548 K, 1573 K, and 1598 K [1250 °C, 1275 °C, 1300 °C, and 1325 °C]) typical for iron ore sintering. The gas atmospheres include a 1 pct CO-24 pct CO$_2$-75 pct Ar mixture which gives an equilibrium pO$_2$ of 2.9×10^{-6} kPa (1523 K [1250 °C]), 5.9×10^{-6} kPa (1548 K [1275 °C]), 1.2×10^{-5} kPa
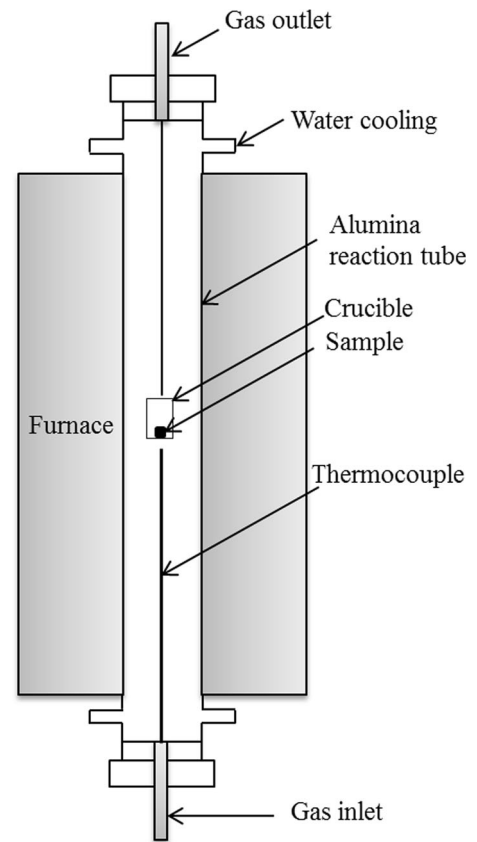

Fig. 1—Schematic of the sintering apparatus.

Table I. The Major Chemical Compositions of Raw Materials, Weight Percent

Raw Material	Total Fe	CaO	SiO$_2$	Al$_2$O$_3$	MgO	TiO$_2$	Loss on Ignition
Iron ore blend	58.46	2.77	5.46	1.67	0.58	0.09	
Limestone	0.15	54.08	1.48	0.35	0.37		43.1
Dolomite	0.58	29.92	1.16	0.28	20.11		46.3
Silica sand	0.49	1.58	92.4	1.71	0.23		1.3
Ironsand*	58.28	0.59	2.34	3.78	3.06	7.95	2.5

* Based on XRF analysis. Table II lists more detailed chemical composition.

(1573 K [1300 °C]), and 2.3×10^{-5} kPa (1598 K [1325 °C]). A pO_2 of 0.5 and 5 kPa was achieved by mixing Ar and air, and pO_2 of 21 kPa by using air.

To conduct the experiments, the furnace was pre-heated to a designated temperature, and then purged with the desired gas mixture for at least 20 minutes. The crucible with the specimen tablet(s) was then placed in the hot zone of the furnace. After sintering for the desired time (between 5 and 20 minutes), the samples were then rapidly removed from the hot zone to the cool top part of the furnace for quenching in the sintering atmosphere.

C. Characterization of Raw Materials and Sintered Samples

A detailed structure and compositional analysis of the original ironsand was conducted using combined SEM, X-ray fluorescence (XRF), qualitative and quantitative X-ray diffraction (XRD), and electron probe microanalysis (EPMA) techniques. The sintered samples as well as an industrial sinter with the addition of 3 wt pct of ironsand were subjected to optical microscopy and SEM/EDS analysis to observe and characterize the sintering behavior of the ironsand.

1. Optical and SEM/EDS analyses

The sintered samples were mounted in epoxy resin in preparation for optical and SEM analysis. After curing, the basal part of each sample mount was sectioned to expose a fresh surface cross-section. The newly exposed surface was polished to a 1 μm finish for optical microscopic observation (Leica DM6000 Optical Microscope). The polished sample was then carbon coated prior to analysis by field emission scanning electron microscopy (FESEM, JEOL JSM—7001F) operated at 15 kV.

2. X-ray Fluorescence (XRF) Spectroscopy and X-ray Diffraction

Bulk chemical analysis of the ironsand sample was carried out by XRF, performed using a Philips PW2404 XRF spectrometer on glass beads prepared using a lithium tetraborate: metaborate flux. XRD data were collected using a Philips X'Pert diffractometer, fitted with a Cobalt long-fine-focus tube operated at 40 kV and 40 mA and a curved graphite post-diffraction monochromator. A Rietveld refinement-based approach to quantitative phase analysis (QPA)[9] was performed using TOPAS (Version 4.2).[10] In order to determine the absolute phase concentrations via the QPA, the ironsand sample was mixed with an ultrapure and highly crystalline corundum (α-Al_2O_3; Baikalox Alumina Polishing Powder, Type GE6) internal standard.

3. Electron Probe Microanalysis (EPMA)

Two types of EPMA information were obtained. The ironsand sample was first mapped using a high-resolution Field Emission Gun (FEG) equipped EPMA (JEOL 8500F Hyperprobe). This was done in order to

(1) determine the distribution of major and minor mineral phases within the sample[11,12] and, (2) examine the chemical homogeneity of the titanomagnetite grains. Operating conditions for the microprobe during mapping were an accelerating voltage of 15 kV, a beam current of 100 nA, a step size of 2 μm (in x and y), and a counting time of 30 ms per step. The element distribution data obtained by mapping were manipulated using the software package CHIMAGE[13] which incorporates an automated clustering algorithm that identifies chemically alike phases.[14] These phases were then overlaid onto the mapped region to provide a "phase-patched" map showing the distribution of all chemical/mineral phases within the mapped area.

Following mapping by FEG-EPMA, the sample was further examined by quantitative EPMA techniques using a JEOL 8900 Superprobe to assess the distribution of major and minor elements within the titanomagnetite grains. Approximately, 500 randomly selected Ti-bearing grains were analyzed, with the analysis position within each grain also being random. For the quantitative analyses, the microprobe was operated at 15 kV and 40 nA and the electron beam defocused to 10 μm (to account for any within-grain inhomogeneity). Counting times were 20 s on the main peak and 10 s on the background. The suite of elements analyzed included Al, Cr, Mn, Mg, Ti, V, Fe, Si, and Nb. Oxygen was calculated by difference, based on valence.

Table II. Summary of XRF Assay Data and EPMA Results (Weight Percent Unless Otherwise Noted) from 508 Grains for the Ironsand

Oxide	XRF Assay[†]	EPMA Titanate Dataset[‡]
Fe_{tot}	58.3	n.d.^
FeO	35.99*	34.02*
Fe_2O_3	43.36*	48.43*
TiO_2	7.95	8.54
SiO_2	2.34	0.27
Al_2O_3	3.78	3.48
MgO	3.06	3.09
CaO	0.59	n.d.
MnO	0.64	0.74
Cr_2O_3	0.045	0.072
Nb_2O_5	n.d.	0.002
ZrO_2	0.011	n.d.
P_2O_5	0.077	n.d.
K_2O	0.024	n.d.
ZnO	0.086	n.d.
U (ppm)	20	n.d.
Th (ppm)	<DL	n.d.

[†]Detection limits are 0.005 wt pct except for MgO, Cr_2O_3, U, and Th where the detection limits are: 0.01 wt pct, 0.002 wt pct, 10 ppm, and 10 ppm, respectively.

[‡]Data exclude any impurity grains (e.g., quartz, aluminosilicates, etc.) that were present in the sample.

n.d. not determined.

* Calculated using the method of Droop[16] for estimating the Fe^{3+} concentration in spinels using stoichiometric criteria.

III. RESULTS

A. Characterization of the Ironsand

1. Bulk Composition

Table II lists the bulk composition of the ironsand as determined by XRF analysis. The ironsand contained 7.95 wt pct TiO_2 and 58.3 wt pct total Fe. It is well known that the titanomagnetite ore from New Zealand is a solid solution of magnetite and ulvöspinel as expressed as $(Fe_3O_4)_{1-x}(Fe_2TiO_4)_x$ or $(FeO.Fe_2O_3)_{1-x}(2FeO.TiO_2)_x$.[15]

FeO and Fe_2O_3 components were calculated using the method of Droop[16] for estimating the Fe^{3+} concentration in spinels using stoichiometric criteria. Using these derived FeO and Fe_2O_3 molar fractions, the method of Jung[17] for calculating the molar fraction of ulvöspinel in titanomagnetite gives $x = 0.27$. This is in excellent agreement with 0.27±0.02 previously determined by Park and Ostrovski[15] and with 0.28 recently determined by Jung.[17]

Major impurities in the bulk concentrate included Al_2O_3 3.78 wt pct, MgO 3.06 wt pct, SiO_2 2.34 wt pct, V_2O_5 0.607 wt pct, and MnO 0.638 wt pct. The impurities aluminum, vanadium, manganese, and magnesium were typically associated with the titanomagnetite grains, occurring as solid solution components within the lattice. The other impurity elements, including some aluminum, were more typically associated with gangue mineral grains such as aluminosilicates (*e.g.*, pyroxenes, feldspars, and clays), quartz, and apatite.

2. Ironsand morphology

Figure 2(a) and (b) presents two optical micrographs of original ironsand particles. The two morphological types present include homogeneous particles and those with exsolution lamellae, respectively. Cocker *et al.*[1] examined New Zealand ironsands using EPMA and found that homogeneous titanomagnetite particles that were relatively rich in Ti, (containing up to 8.2 wt pct TiO_2), accounted for 90 to 95 vol pct of the ironsands. In the particles exhibiting the exsolution lamellae structure, the lighter regions of variable thickness in a trellis-like pattern were of hematite-ilmenite composition with an overall high TiO_2 content of 13.1 wt pct, while the titanomagnetite host was relatively low with about 1.5 wt pct TiO_2.

The optical micrograph of a typical ironsand particle after heating in air at 1473 K (1200 °C) for 5 minutes is presented in Figure 2(c). After heating, the coarsened hematite-ilmenite exsolution lamellae were present in the majority of ironsand particles. High-temperature oxidation of Fe^{2+} to Fe^{3+} in titanomagnetite produces vacancies in octahedral sites of the {111} crystal planes, allowing increased diffusion of Ti to these regions which led to the formation of hematite-ilmenite lamellae (1 to 10 μm) along the original {111} planes of the titanomagnetite host.[18] The extent of oxidation of the titanomagnetite particle is determined by kinetics. Wright[19] reported that virtually complete oxidation of ironsand to titanohematite was achieved on heating in air at 1073 K (800 °C) for 2 h.
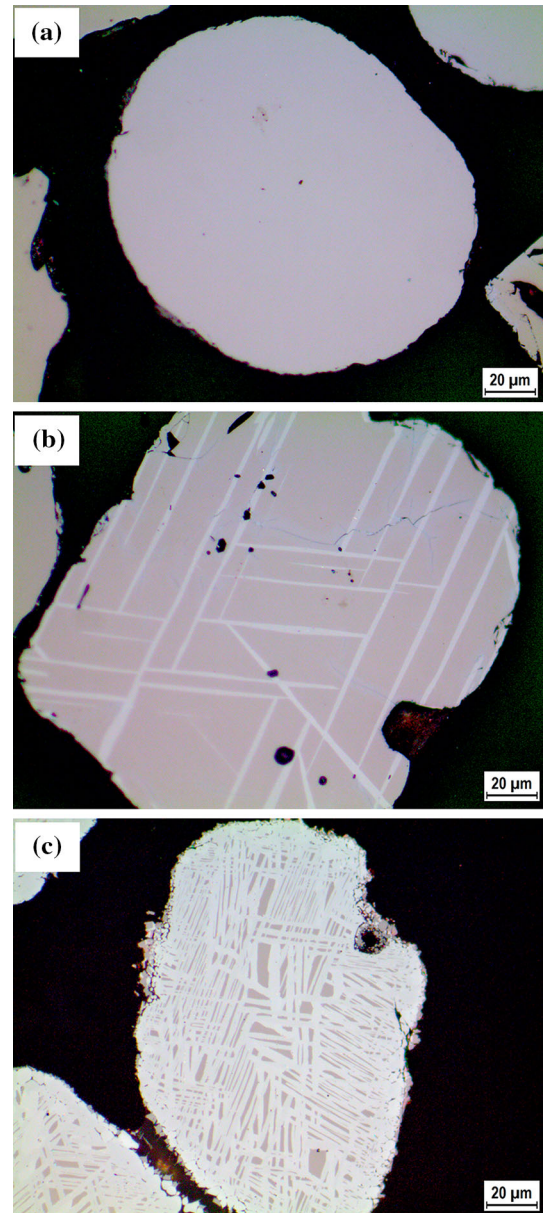

Fig. 2—Optical micrographs of typical ironsand particles. Image (*a*) shows a homogeneous titanomagnetite particle (uniform pink). Image (*b*) is a titanomagnetite particle with thick hematite-ilmenite (white bands) exsolution lamellae. Image (*c*) shows that ironsand particles heated in air at 1473 K (1200 °C) for 5 min exhibiting an increase in the amount of exsolution lamellae present.

3. XRD

Qualitative phase analysis showed that the ironsand contained a spinel phase which, based on the EPMA analysis, was designated titanomagnetite, an intermediate member of the isomorphous series of solid solutions of magnetite ($FeFe_2O_4$) and ulvöspinel (Fe_2TiO_4), with a nominal composition of $Fe_{2.75}Ti_{0.25}O_4$ (ICDD card no. 01-075-1374). Peaks for ilmenite ($FeTiO_3$, 29-0733), hematite (Fe_2O_3, 33-0664), and quartz (SiO_2, 33-1161) were also observed. For the Rietveld refinement-based QPA, the crystal structure data of Bosi *et al.*,[20] Wechsler and Prewitt,[21] Blake *et al.*,[22] Lager *et al.*,[23] and Brown *et al.*[24] were used for titanomagnetite,
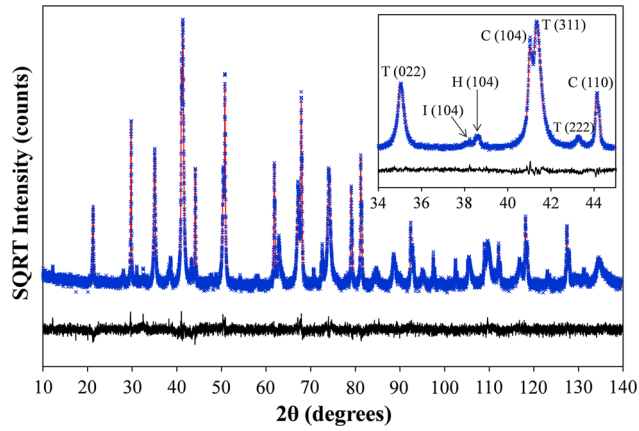
Fig. 3—Rietveld refinement fit for the XRD data collected for the ironsand/corundum mixture. Experimental data are shown as crosses, the calculated pattern as a solid line and the difference pattern as a solid line below. R_{wp} = 9.14; R_{exp} = 7.05. The inset shows the range 34 deg $\leq 2è \leq 45$ deg, with reflections from titanomagnetite (T), ilmenite (I) and hematite (H) annotated on the plot. C = the corundum internal standard.
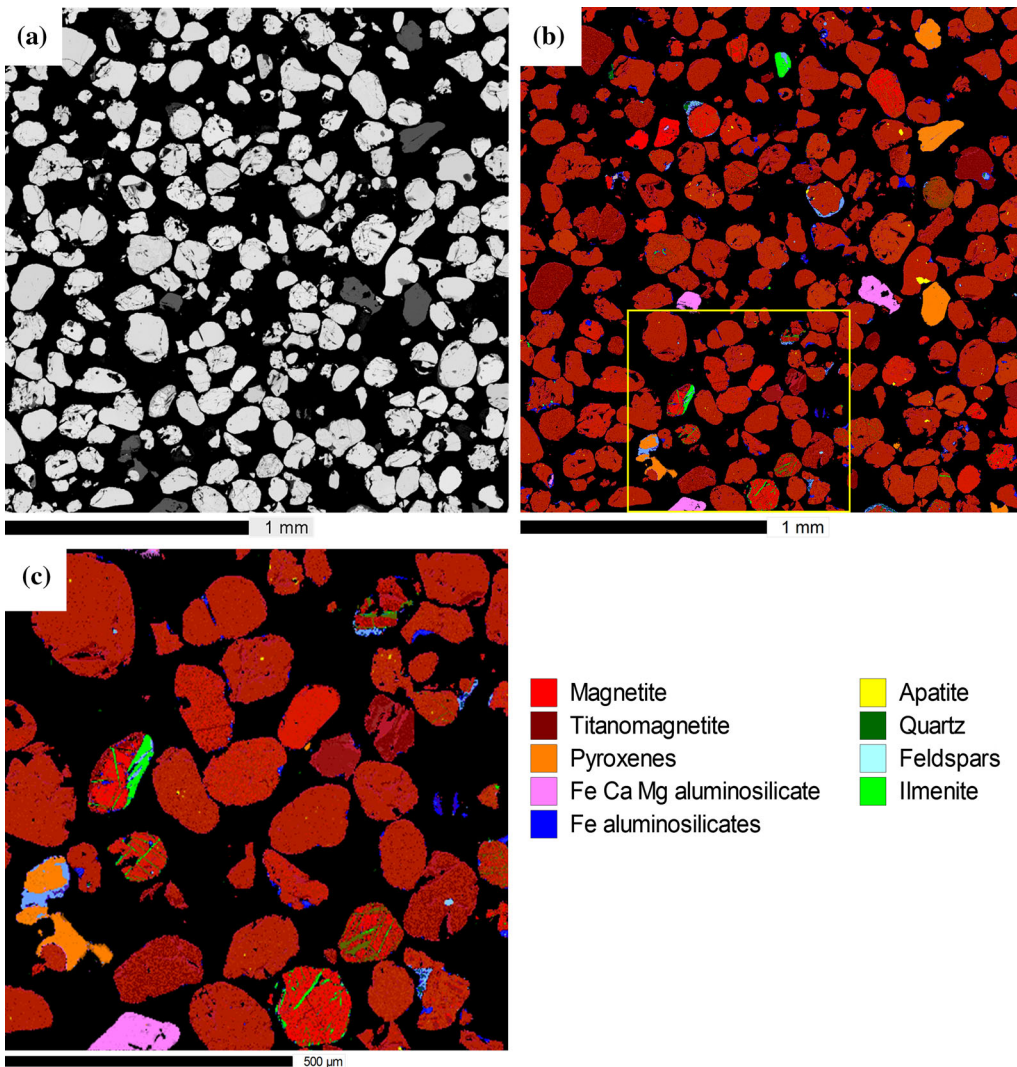

Fig. 4—EPMA mapping results for the ironsands. Image (a) is a BSE image of the mapped area. Titanomagnetite grains appear bright in BSE contrast, while gangue aluminosilicate grains are darker. Image (b) is the phase distribution map for the area shown in the BSE image. Image (c) is a magnified view (boxed region shown in image (b)) highlighting the Ti-rich lamellae within individual magnetite and titanomagnetite particles.

ilmenite, hematite, quartz, and corundum, respectively. Figure 3 shows the Rietveld refinement output for the ironsand/corundum mixture; the inset shows clearly the peaks from the crystalline phases. The absolute phase abundances were 84.1, 1.7, 3.0, and 0.5 wt pct for titanomagnetite, ilmenite, hematite, and quartz, respectively. Therefore, there was 10.7 wt pct unidentified material, comprised mainly of the pyroxene, aluminosilicates, apatite, and feldspar phases as identified by EPMA.

4. EPMA mapping

The results from the EPMA mapping are shown in Figure 4 in the form of (a), a BSE image showing all grains within the mapped area, and (b) a map showing the types and distribution of phases within the mapped area. Figure 4(c) shows a magnified view (boxed region shown in image (b)) highlighting the Ti-rich lamellae within individual magnetite and titanomagnetite particles. The sample comprises >80 to 85 pct titanomagnetite with associated gangue minerals including ilmenite, pyroxenes (a mixture of enstatite and diopside), unidentified Fe/Ca/Mg, and Fe-rich aluminosilicates and minor to trace amounts of quartz, apatite, and feldspar. The majority of gangue mineral grains are largely fully liberated except for the feldspars and Fe-rich aluminosilicate which are present as pore-fill or coatings on titanomagnetite.

5. Quantitative EPMA

To characterize the composition of the titanomagnetite component of the New Zealand ironsand, quantitative EPMA analyses on individual Ti-rich grains within the sample were undertaken. A comparison of the bulk assay determined *via* XRF for these samples with the bulk average analyses is provided in Table II.

To examine variation in the composition of the Ti-rich grains, the EPMA data were plotted on a Ti *vs* Fe scatter plot (Figure 5). The data lie on an extended composition range from 0 at pct Ti (magnetite or hematite dominated compositions) to ~20 at pct Ti (ilmenite) with a cluster of data points centered close

to 5 at pct Ti and 30 at pct Fe corresponding to titanomagnetite. The average atomic Fe/Ti ratio of the ironsand concentrate based on the data in Table II (column 2) was 9.26. Major impurities within the titanomagnetite grains consisted of, on average, Al_2O_3 3.48 wt pct, MgO 3.09 wt pct, MnO 0.74 wt pct, and V_2O_5 0.51 wt pct. Excluding the high Ti-containing particles and any gangue mineral grains, the atomic Fe/Ti ratio of the titanomagnetite grains only was increased to 9.28. This gave a calculated ulvöspinel fraction in the homogeneous titanomagnetite solid solution $(Fe_3O_4)_{1-x}(Fe_2TiO_4)_x$ of 0.27.

B. Characterization of Relict Ironsand in Industrial Sinter

Figure 6 presents the optical micrographs of two relict ironsand particles taken from two pieces of an industrial sinter which are assumed to have experienced different sintering conditions. It is known that the temperature and gas atmosphere during the sintering process are far from homogeneous. Generally, during the heating stage, iron oxides adjacent to the coke particles are sintered at a higher temperature and lower oxygen partial pressure, and therefore are easier to reduce to magnetite. In contrast, primary hematite particles present after sintering have remained separated and relatively far from

Fig. 6—Optical micrographs of two typical relict particles of New Zealand ironsand in the industrial sinter. Image (*a*) indicates a relatively oxidizing environment, whereas image (*b*) shows results from a more reducing environment. H: Hematite; M: Magnetite; S: Silicates; I: Ironsand.
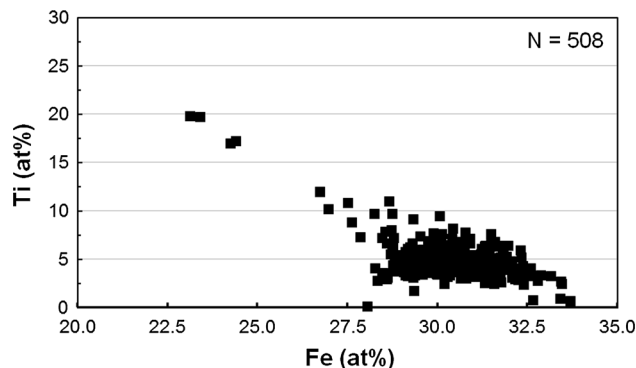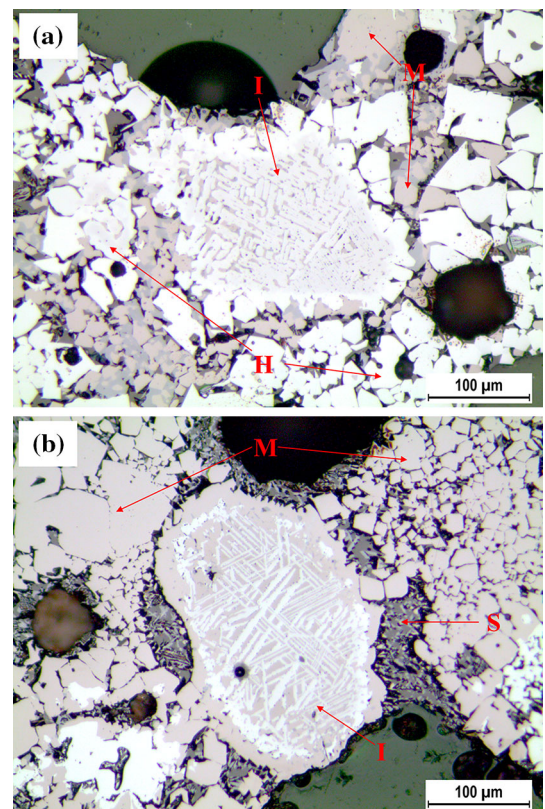

Fig. 5—Quantitative EPMA results showing the relationship between Fe and Ti in the Ti-containing grains. Titanomagnetite compositions plot as a cluster centered around 5 at pct Ti, 30 at pct Fe. More Ti-rich compositions represent possible ilmenite and altered titanomagnetite components (alteration is usually associated with leaching of Fe).

the coke. During the cooling stage, any magnetite particles adjacent to open pores are easily oxidized to secondary hematite, while other materials that are distant from open pores may still be present in an atmosphere of low oxygen potential and remain in their reduced form.[25]

Figure 6(a) shows a typical ironsand particle sintered in a relatively oxidizing atmosphere as indicated by the abundance of secondary hematite in the surrounding solid. The particle can be identified by its characteristic morphology with the internal structure having the typical lamellae texture similar to that given in Figure 2. The boundary of the ironsand particle however became less distinct with the lamellae-textured core surrounded by a layer of smaller, secondary hematite crystals. The oxidation of the ironsand particle resulted in the development of the coarsened hematite-ilmenite lamellae. Figure 6(b) shows another typical ironsand particle in the industrial sinter, where a clear boundary with surrounding silicate (glass) phase and magnetite crystals can be seen. The lack of hematite and abundance of associated magnetite indicated that the ironsand particle experienced relatively reducing sintering conditions. In this case, a magnetite-rich rim was present around the periphery of the ironsand particle as a result of reduction (although this process was not complete as demonstrated by the presence of a more oxidized core region).

Figure 7 shows a BSE image and element distribution maps of a lightly reacted particle of ironsand in industrial sinter. In this example, exsolution took place in the interior of the particle causing enrichment of Ti in the titanohematite phase and incorporation of Mg and Al in the titanomagnetite host. Meanwhile, the periphery was reduced forming a magnetite rim that was richer in iron but had less Ti, Mg, and Al in comparison to the interior. These elements diffused outwards and entered the surrounding silicate phase. Upon solidification, Mg entered into crystallized magnetite leaving a silicate phase with little Mg. It is also noted that a phase rich in Ti and Ca was distributed between the core of the ironsand particle and its reduced magnetite periphery layer. A phase with a similar composition was observed adjacent to a void in the particle where Ca and Ti contents were high. These small zones were described as being perovskite phase, $CaTiO_3$, incorporating some silica (with Si content 0.13 to 1.24 at pct, mostly less than 1 at pct).

Figure 8 shows a BSE image and element distribution maps from a region of industrial sinter that was distant from relict ironsand particles. The columnar SFCA phase was associated with magnetite and glassy phase in this region. Most Ti was concentrated in the glassy phase. Point analysis by EDS showed that the slag phase consisted of 19.7 at pct calcium, 15.8 at pct silicon, 4.36 at pct iron, and 1.54 at pct titanium. The titanium content in the slag phase was slightly higher than that
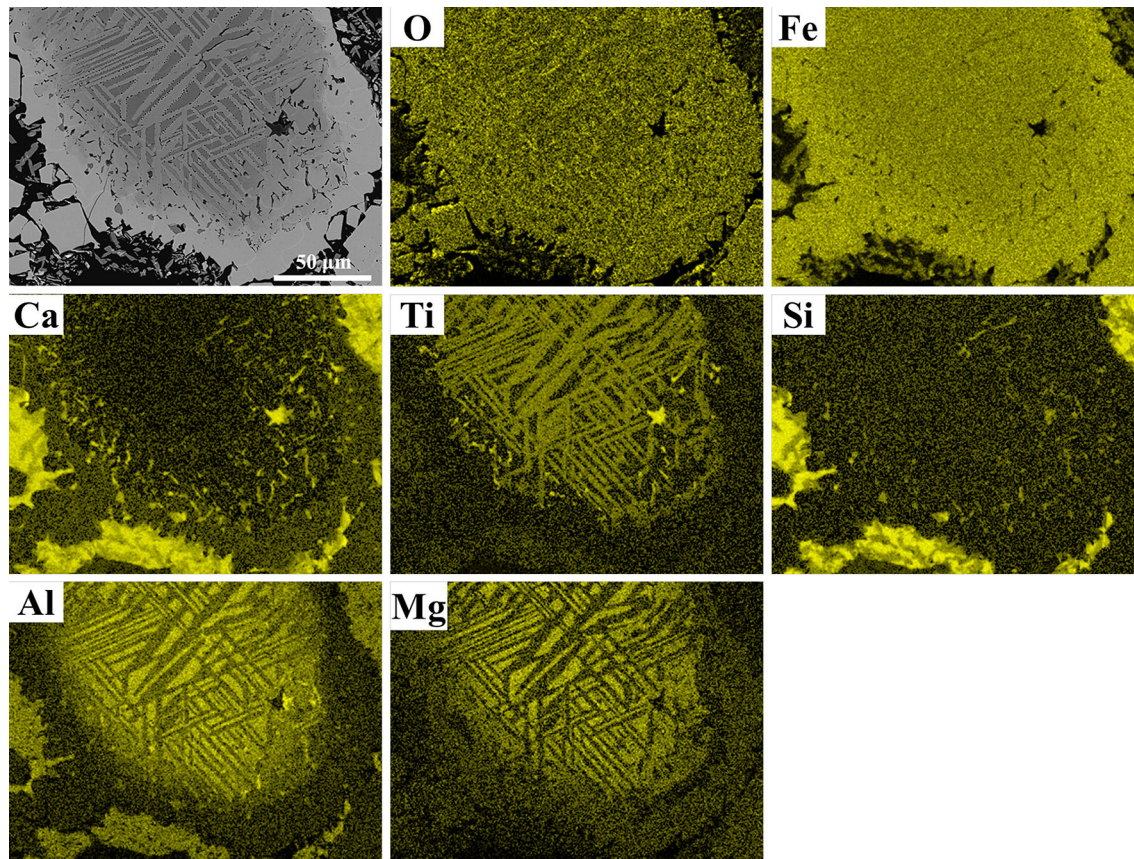

Fig. 7—BSE image and EDS mapping of a typical relict ironsand particle in the industrial sinter.
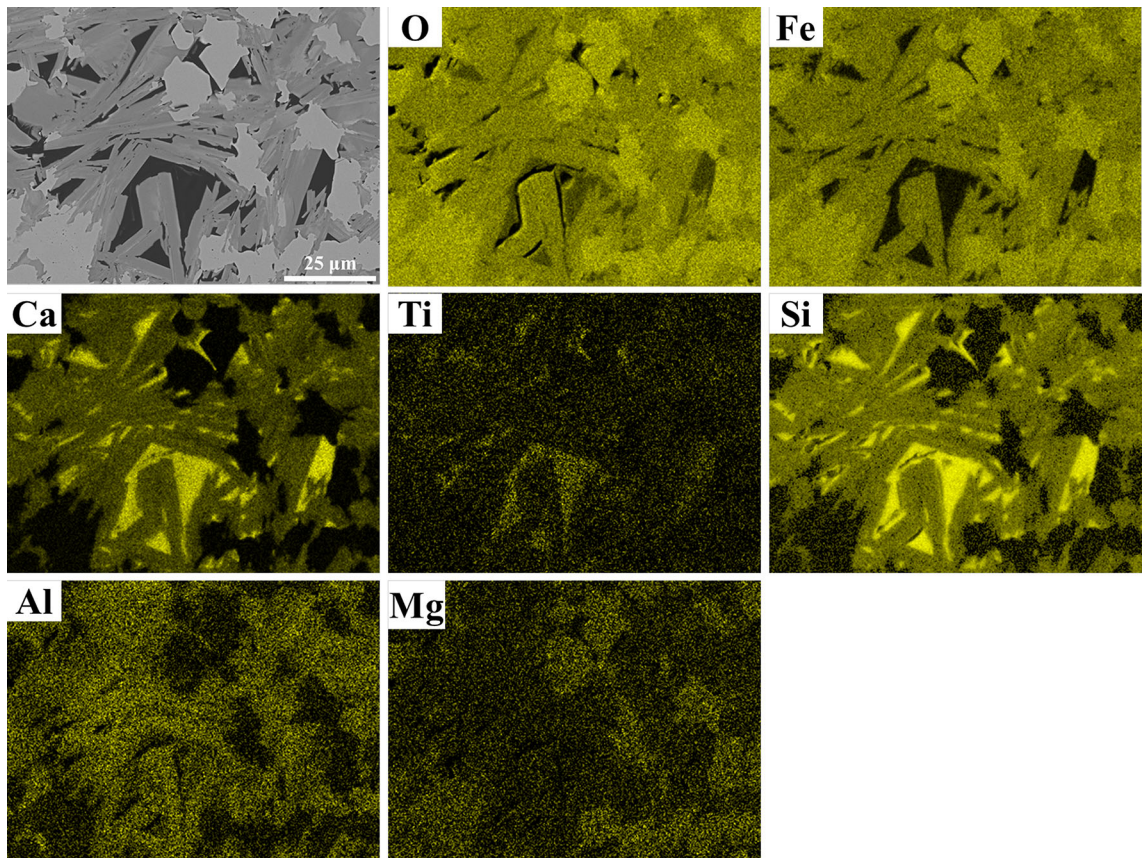
Fig. 8—BSE image and EDS mapping of matrix phases in the industrial sinter. The BSE image shows typical textures exhibited by SFCA (medium gray phase), slag (or glass phase—darkest phase, rich in Ca and Si and also with elevated Ti), and magnetite (brightest phase).

obtained by Bristow and Loo[4] who used a similar amount of ironsand addition. Mg was concentrated in the magnetite phase but Al was selectively concentrated in the SFCA phase.

C. Bench-scale Sintering of Iron Ore Mixes Containing New Zealand Ironsand

To better understand the behavior of New Zealand ironsand during sintering, an iron ore blend with 5 wt pct of ironsand was sintered under different conditions (*i.e.,* variable T and pO_2), and the specimens were examined by optical microscopy and SEM. Here, the focus is exclusively on the behavior of the ironsand during the sintering process. A quantitative examination of the formation of mineral phases will be reported separately.

Figure 9 shows the effect of sintering temperature and gas atmosphere on the extent of sintering. The extent of coalescence of particles in the starting raw mixture increased gradually with increasing sintering temperature. Figure 9(a) shows the microstructure of a sample sintered at 1523 K (1250 °C) for 4 minutes in a gas mixture containing CO 1 pct, CO_2 24 pct, and Ar 75 pct. There was distinct aggregation of the sample and reactions between the fine particles resulted in the generation of SFCA in addition to the reduction of almost all hematite into magnetite. At this temperature,

the assimilation of oxide materials was incomplete, leaving a large proportion of only partially reacted iron ore and flux particles. Secondary magnetite crystals which were segregated from melt phase were rarely found in the specimen. The major change of the ironsand was exsolution of a titanohematite phase to form the lamellae texture. Interaction of the ironsand particles with other components was also not obvious.

When the sintering temperature was increased to 1573 K (1300 °C) (Figure 9(b)), it was found that more significant aggregation of fine particles took place, forming fewer but larger pores. The specimen was dominated by polycrystalline magnetite distributed in a continuous silicate matrix. As expected, no SFCA was observed in the specimen. A layer on the periphery of the ironsand particles was reduced to magnetite with which assimilation took place and caused some boundaries to become vague. Figure 9((c) through (e)) presents the microstructure of samples heated at 1573 K (1300 °C) for 4 minutes in the gas atmospheres with pO_2 = 0.5, 5, and 21 kPa, respectively. Consistent with the recent results of Webster *et al.*,[26,27] increasing O_2 partial pressure resulted in more SFCA. In the sample sintered in air (Figure 9(e)), SFCA was the dominant phase with significant amounts of hematite. Magnetite was rarely observed under these conditions. In all of the samples, ironsand boundaries were clearly visible although intimately bonded with surrounding phases.
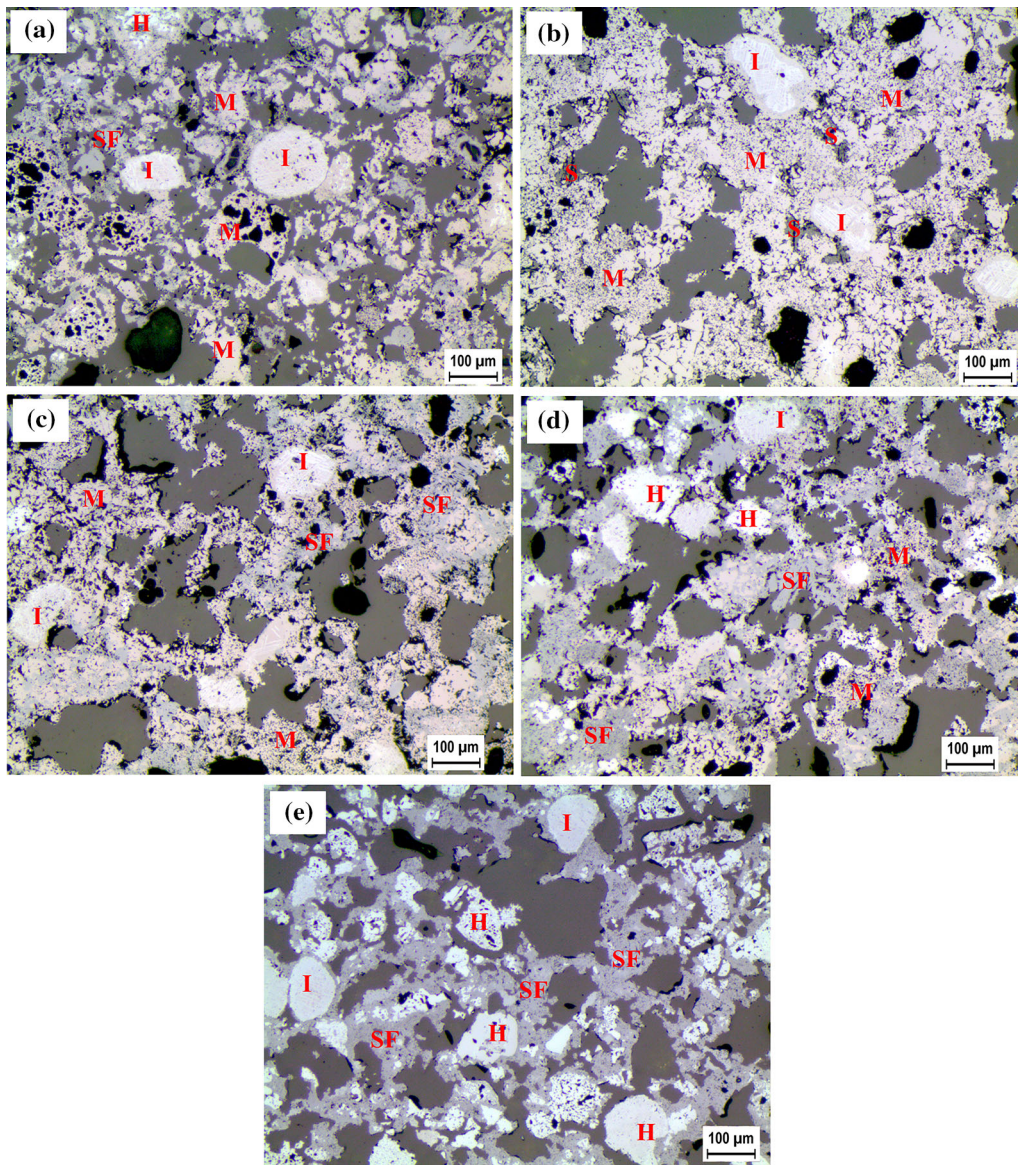
Fig. 9—Optical micrographs of specimens sintered for 4 min at different temperatures in various gas atmospheres. H: hematite; M: magnetite; SF: SFCA; S: silicates; I: ironsand. (*a*) 1 pct CO, 1523 K (1250 °C); (*b*) 1 pct CO, 1573 K (1300 °C); (*c*) 0.5 pct O$_2$, 1573 K (1300 °C); (*d*) 5 pct O$_2$, 1573 K (1300 °C); (*e*) air, 1573 K (1300 °C).

Figure 10 consists of four optical reflected light images of typical ironsand particles in samples sintered under the different conditions. The morphology of the relict ironsand particle in the sample sintered at 1523 K (1250 °C) in a gas atmosphere with pO$_2$ = 0.5 kPa for 20 minutes (Figure 10(a)) was similar to that in the industrial sinter shown in Figure 6(b). The ironsand particles were reduced in the periphery and bonded with surrounding magnetite without complete assimilation. Increasing sintering temperature to 1573 K (1300 °C) resulted in complete reduction of the titanohematite phase because the lamellar texture completely disappeared. Only the contour of the ironsand particles could be identified (the oval in Figure 10(b)).

Different morphologies of ironsand particles can be found in samples sintered in air, as shown in

Figure 10(c) and (d). In these experiments, the presence of the ironsand particles is much easier to identify due to remaining titanohematite lamellae structure, although the bonding between them and surrounding oxides increased with increasing sintering temperature. As shown in Figure 10(d), a significant amount of SFCA phase was formed at 1573 K (1300 °C) in air, although no SFCA phase was detected in a mixture with 0.5 pct O$_2$ at the same temperature.

Figure 11 shows a typical ironsand particle in the sample heated at 1523 K (1250 °C) for 20 minutes in a gas atmosphere with pO$_2$ = 0.5 kPa. A reaction zone, which contained a high level of Ca and Ti and a relatively low level of Fe between the core with the characteristic lamellae structure and the reduced magnetite periphery layer, was established. This zone was
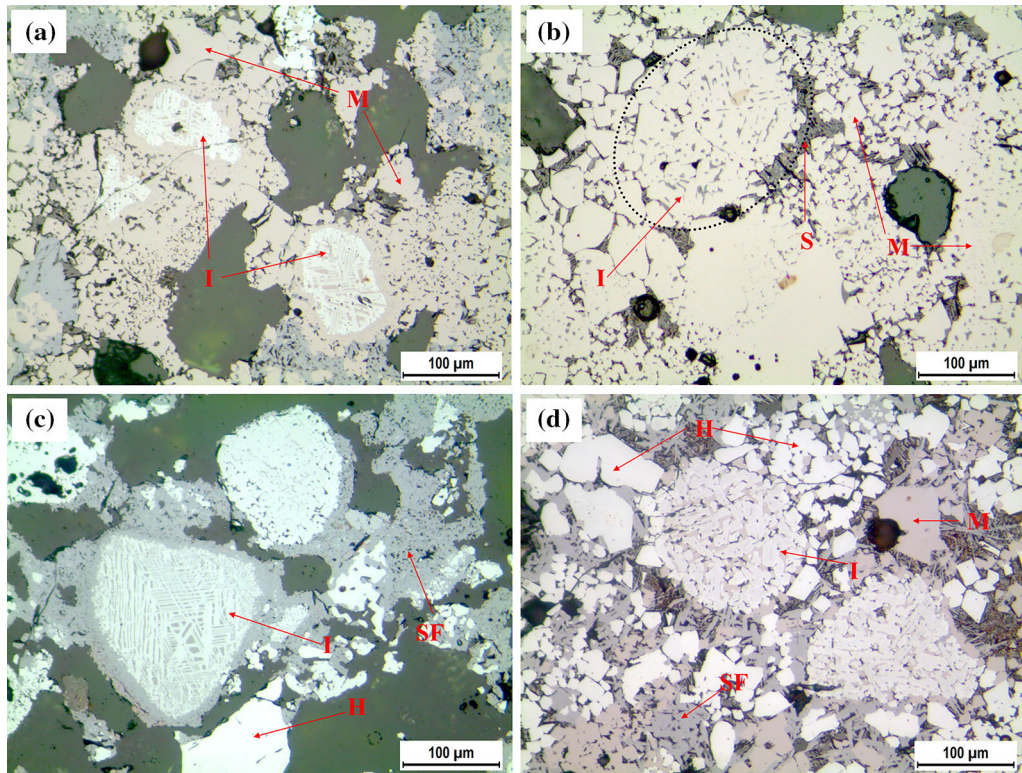
Fig. 10—Optical micrographs of typical ironsand particles in specimens sintered at different temperatures for 20 min in different gas atmospheres. (*a*) 0.5 pct O_2, 1523 K (1250 °C); (*b*) 0.5 pct O_2, 1573 K (1300 °C); (*c*) air, 1523 K (1250 °C); (*d*) air, 1573 K (1300 °C).
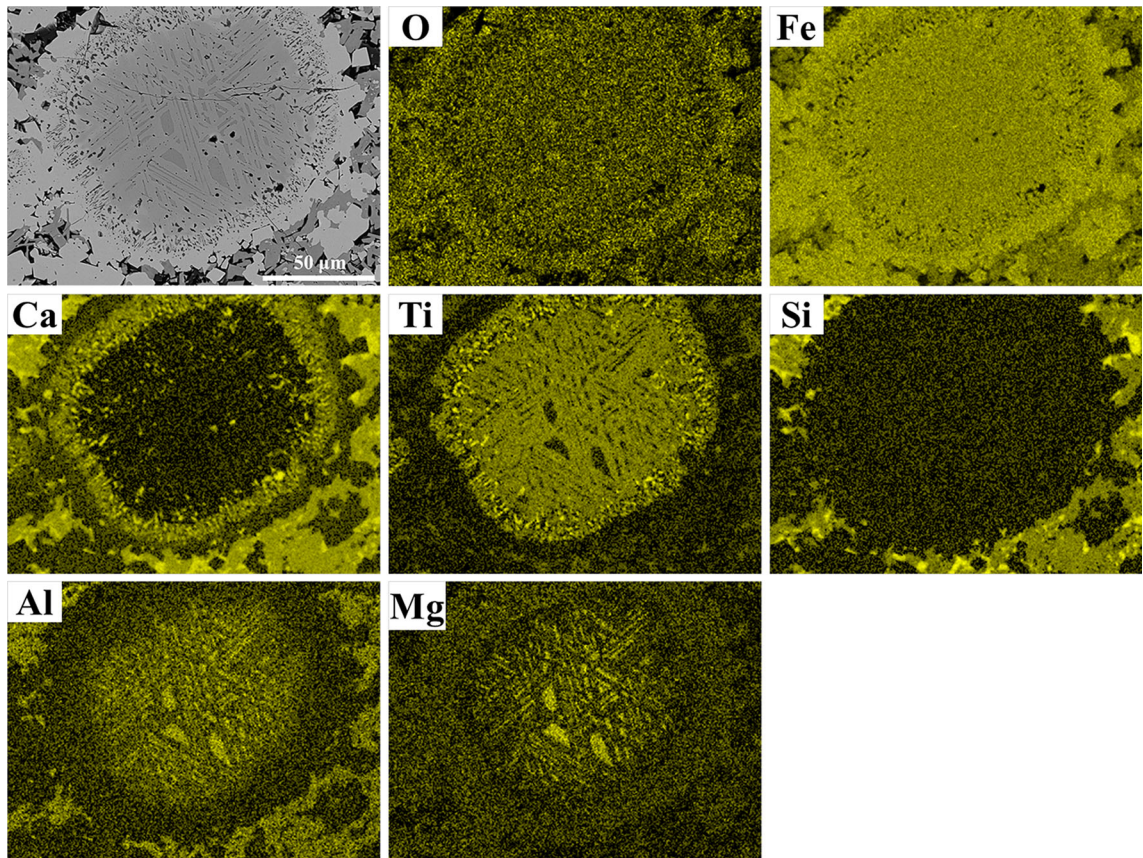

Fig. 11—BSE image and EDS mapping of a typical relict ironsand particle in a specimen sintered at 1523 K (1250 °C) for 20 min in the gas atmosphere with pO_2 = 0.5 kPa.

similar to that observed in the industrial sinter shown in Figure 7, but with a more established intermediate layer which was attributed to the extended sintering time that allowed more CaO diffusion into the particle interior.

A detailed EDS analysis across the reaction zone of the same ironsand particle was performed. The compositions of different points presented in Figure 12 across the reaction zone and beyond are listed in Table III. Points 1 and 2 represent the phase composition of the Ti-lean titanomagnetite matrix and the Ti-rich hematite-ilmenite lamellae within the relict ironsand, respectively. The dark, finely distributed areas within the reaction zone as represented by points 3 and 4 were identified to be a complex perovskite phase containing Fe in addition to CaO and TiO_2 which is also found in Figure 7. Point 5 was from the magnetite rim of the ironsand particle which characteristically contained some CaO and MgO. Additional phases surrounding the ironsand particle included silicate glass (points 6 and 7), secondary magnetite (point 8), and SFCA (points 9 and 10). Besides in the relict ironsand particle, titanium was also found in the silicate phase (1.8 to 2.2 at pct)
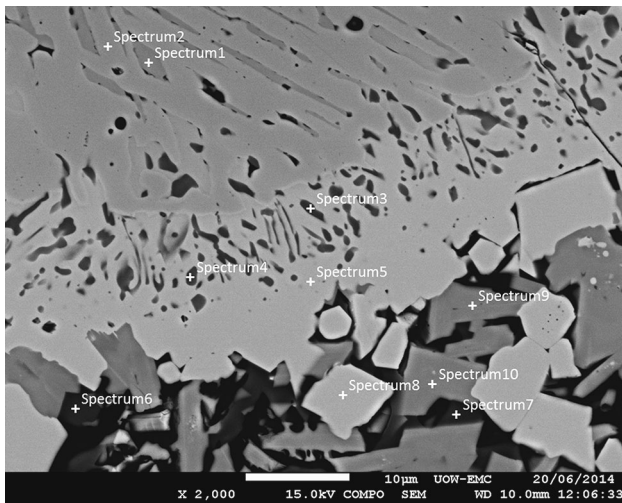

Fig. 12—The BSE image of the reaction zone of a typical ironsand particle in a sample heated at 1523 K (1250 °C) for 20 min in the gas atmosphere with pO_2 = 0.5 kPa.

and SFCA (about 0.3 at pct) in close proximity to the relict ironsand particle.

It was recognized that during sintering, when the solid CaO or a silicate melt was in contact with an ironsand particle, TiO_2 diffused outwards, while CaO diffused toward the center of the particle. When the CaO was accumulated to some concentration, it combined with TiO_2 due to their chemical affinity[28] to form the perovskite phase that was finely distributed in the reaction zone of an ironsand particle. The ironsand surface was attacked by the silicate melt and gradually dissolved into the melt. On cooling, secondary magnetite or SFCA phase was segregated from the melt phase making the particle boundary ambiguous.

Figure 13 shows the BSE image and EDS mapping of a typical relict ironsand particle in a specimen sintered at 1573 K (1300 °C) for 20 minutes in a gas atmosphere with pO_2 = 0.5 kPa. On the BSE image, the ironsand particle can only be identified by its rounded contour and texture, although the boundary had substantially disappeared. However, the presence of perovskite phase as characterized by bright dots on the Ti distribution gave evidence that it was an ironsand particle. Silicate melt penetrated into the matrix of ironsand particles, which enhanced their assimilation. The glass phase present inside the ironsand particle had a similar composition to that outside, containing about 2.1 at pct of Ti. In comparison, the magnetite matrix of the ironsand relict contained less than 0.2 at pct of Ti. The dispersed perovskite phase remaining in the core of the ironsand relict showed that the assimilation of the ironsand particle was not complete.

Figure 14 presents the BSE image and the distribution of the main elements Fe, Ca, Ti, Mg, and Al of an ironsand particle in a specimen sintered in air at 1573 K (1300 °C) for 20 minutes. The distribution of Si appeared identical to that of Ca. Unlike the sample sintered under otherwise the same conditions but lower pO_2 (Figure 13), the assimilation of ironsand with other oxides was limited. Penetration of Ca reached the center of the particle but it was only distributed in the finely fragmented areas associated with Si, Al, and less iron which belong to silicate and SFCA phases. There were two phases with the lamellae structure of ironsand particle, as indicated by the Ti-rich and Mg-rich lamella

Table III.   Elemental Composition (Weight Percent) of Grains Marked in Fig. 12 and Corresponding Phases

Point No.	Fe	Ca	Ti	Si	Al	Mg	Phase Identified
1	64.7 (37.4)	0.29 (0.23)	1.08 (0.73)	0.13 (0.15)	4.47 (5.35)	4.23 (5.62)	titanomagnetite
2	64.2 (38.1)	0.09 (0.07)	6.62 (4.58)	0.12 (0.14)	1.92 (2.36)	1.16 (1.59)	titanohematite
3	19.9 (10.1)	21.7 (15.3)	23.1 (13.7)	0.15 (0.15)	0.40 (0.42)	0.13 (0.15)	perovskite
4	27.1 (14.1)	19.4 (14.1)	19.4 (11.8)	0.08 (0.08)	0.43 (0.47)	0.27 (0.33)	perovskite
5	72.2 (44.4)	1.59 (1.36)	0.25 (0.18)	0.12 (0.14)	0.80 (1.02)	1.15 (1.62)	magnetite
6	12.2 (5.62)	30.1 (19.3)	3.44 (1.85)	16.2 (14.8)	2.88 (2.74)	0.22 (0.23)	silicate (glass)
7	13.7 (6.33)	29.3 (18.9)	4.07 (2.20)	15.8 (14.6)	1.92 (1.84)	0.10(0.10)	silicate (glass)
8	74.5 (47.0)	0.93 (0.82)	0.18 (0.42)	0.10 (0.12)	0.74 (0.96)	1.19 (1.72)	secondary magnetite
9	54.2 (30.2)	10.9 (8.43)	0.65 (0.42)	3.39 (3.76)	3.04 (3.51)	0.43 (0.54)	SFCA
10	55.1 (30.8)	10.8 (8.43)	0.49 (0.32)	3.27 (3.64)	2.78 (3.22)	0.38 (0.49)	SFCA

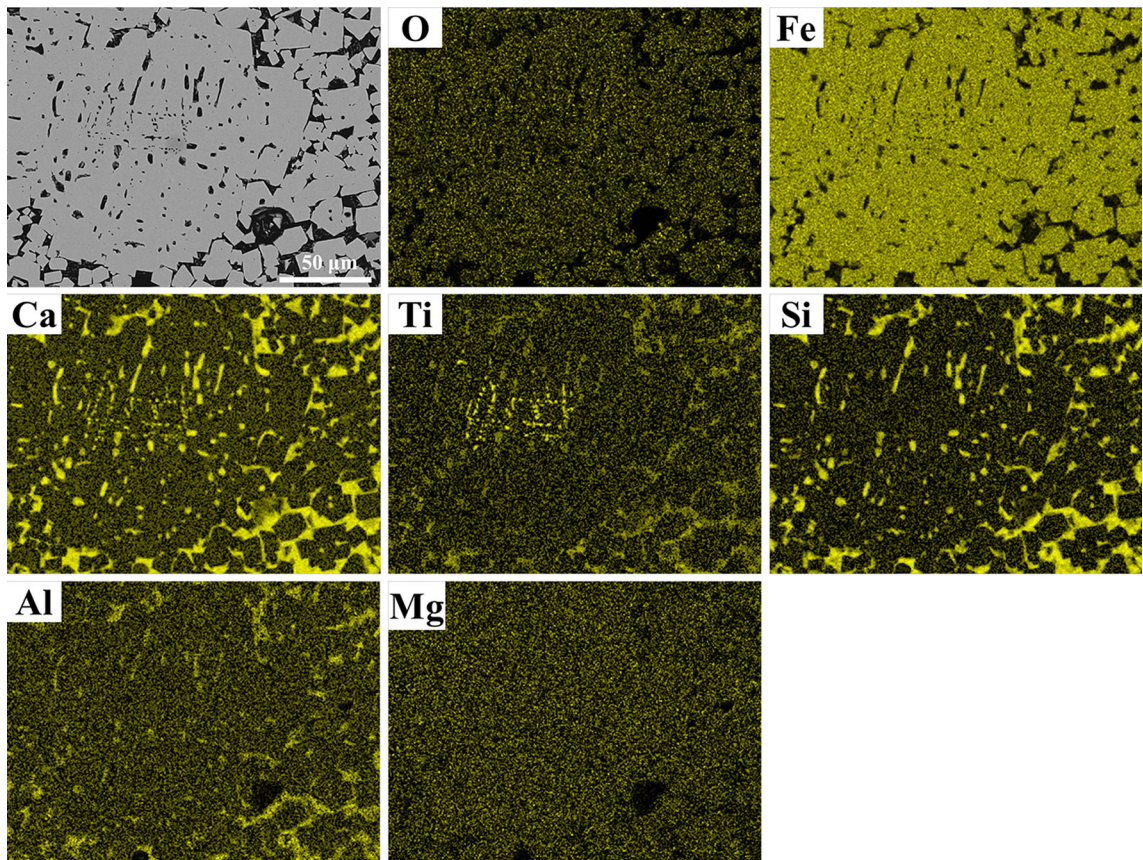The data in brackets are the elemental composition expressed in at pct.

Fig. 13—BSE image and EDS mapping of a typical relict ironsand particle in a specimen sintered at 1573 K (1300 °C) for 20 min in a gas atmosphere with pO_2 = 0.5 kPa.

which were titanohematite and titanomagnetite, respectively. There also existed secondary hematite and magnetite, SFCA, and silicate phases around the relict ironsand particle, and only 0.4 at pct titanium was present in the silicate phase. There was no reaction zone containing dispersed Ca and Fe perovskite phase as was found in ironsand particles sintered in the reducing atmosphere (Figures 11 and 13). In a high oxygen partial pressure atmosphere, the reductive melting of SFCA was suppressed[26], and TiO_2 was stabilized in the titanohematite phase which also inhibited transfer of Ti out of the ironsand particles.

IV. DISCUSSION

In an industrial iron ore sintering process, ironsand particles experience heating, solid reaction, melting, and cooling phenomena. The detailed behavior of an ironsand particle depends on the solid particles in contact with it, as well as the heating history and the prevailing gas atmosphere. Due to the changes of conditions as sintering progresses, the particles also behave differently during sintering.

New Zealand ironsand is primarily present in a titanomagnetite form. Depending on the oxygen potential of the surrounding atmosphere when it is heated, formation of titanohematite exsolution texture can take place to different extents. Along with this process,

elemental redistribution takes place. It was observed in SEM images that Ti tended to concentrate in the titanohematite phase, while its content in the titanomagnetite became lower. In contrast, Al and Mg were selectively concentrated in the titanomagnetite phase (Figures 7, 11, and 14).

When the oxygen potential was low enough, the titanohematite phase decomposed to magnetite, while Ti was segregated from the phase. According to SEM analysis results (Figure 12 and Table III), the Ti content in the magnetite rim formed from an ironsand particle was only 0.18 at pct. Ti was either combined with Ca diffused from outside particles to form a perovskite phase, or diffused into the adjacent silicate phase.

Although the ironsand particles are small, they generally retained their shape after both industrial and laboratory sintering, illustrating that they are more resistant to high-temperature sintering reactions than traditional iron ores. This is especially true for particles which experienced high oxygen potential conditions (Figure 14) where lack of assimilation was particularly obvious and most of the Ti remained in the original ironsand particles. In comparison, ironsand particles which experienced more reducing conditions underwent more assimilation during sintering.

According to Webster et al.,[26] the formation and melting of a low-melting-point phase $CaFe_2O_3$ promoted further sintering by enhancing mass transfer between solid and liquid phases. According to the
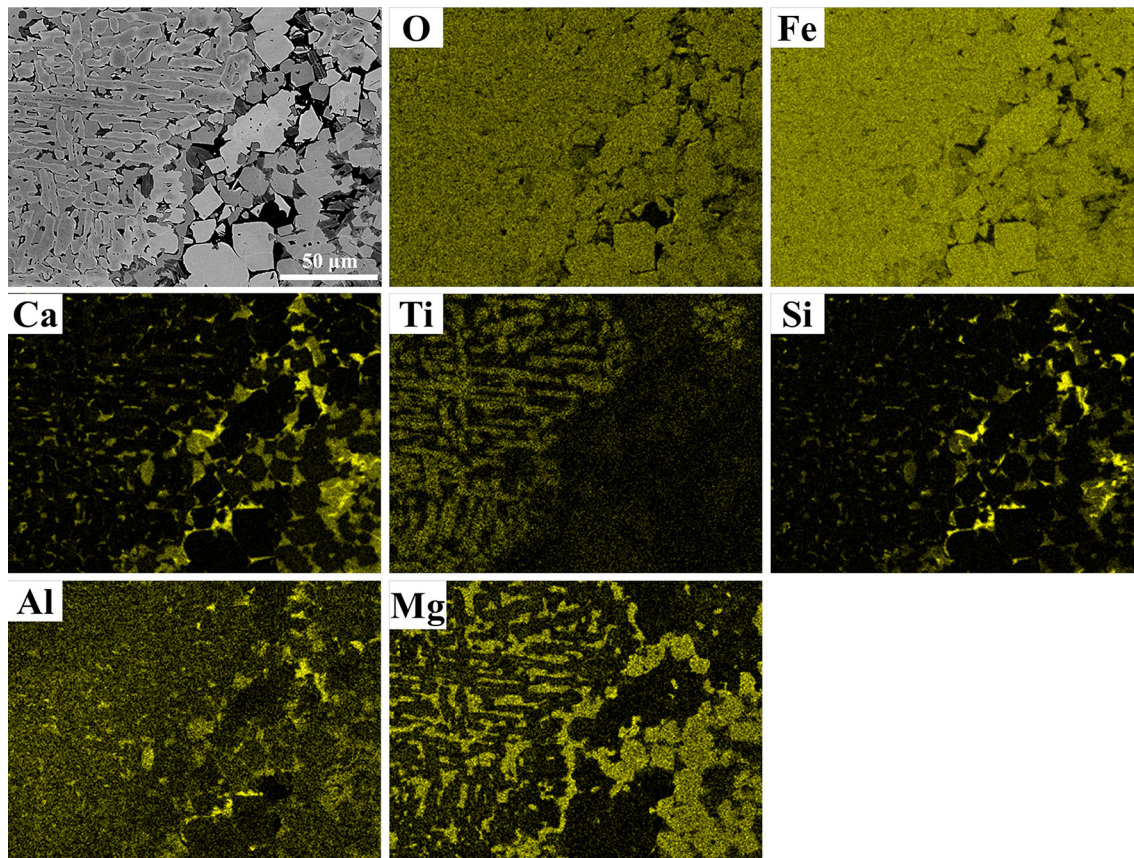
Fig. 14—BSE image and EDS mapping of a typical relict ironsand particle in a specimen sintered at 1573 K (1300 °C) for 20 min in air.
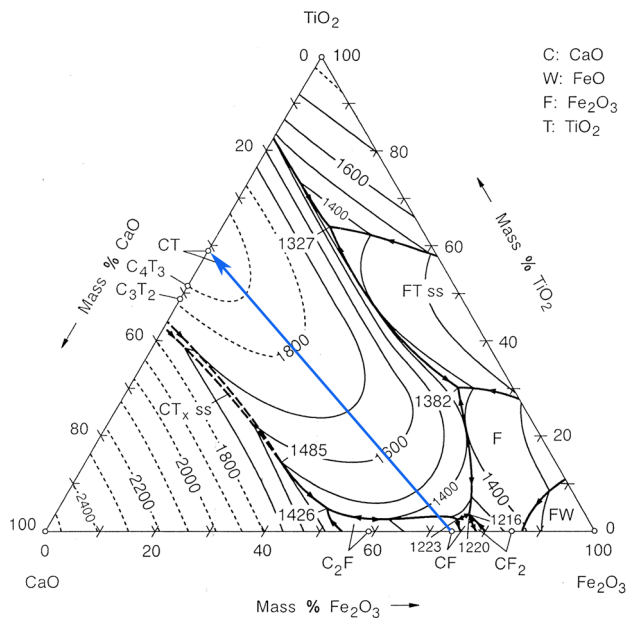

Fig. 15—Liquidus temperature of CaO-TiO$_2$-FeO$_x$ system.[29]

CaO-FeO-Fe$_2$O$_3$ phase diagram,[29] the diffusion of Ca^{2+} into Fe$_3$O$_4$ decreases the melting point of Fe$_3$O$_4$. But Ti existing in the lattice of ironsand can stabilize the

system of CaO-TiO$_2$-FeO$_x$[29] and hinder further dissolution of the ironsand particles. This is illustrated in Figure 15 where the CaO-TiO$_2$-FeO$_x$ phase diagram[29] indicates that the liquidus temperature increases gradually with the introduction of TiO$_2$ along the tie-line from CaO·Fe$_2$O$_3$ (initial melt in iron ore sintering mainly originated from the formation of calcium ferrite) to CaO·TiO$_2$ (blue line in Figure 15).

During cooling, the molten phase segregates into different phases. It is shown in Figures 13 and 14 that Ti preferably remained in the glass phase, while its content in the secondary magnetite, hematite, and SFCA was relatively low. This was also confirmed by the elemental distribution in an industrial sinter as presented in Figure 8.

V. CONCLUSION

In this study, detailed characterization of a raw New Zealand ironsand concentrate and relict ironsand particles in an industrial sinter with 3 wt pct ironsand was conducted. Following these characterization studies, bench-scale sintering experiments were carried out to investigate in detail, the behavior of ironsand during sintering to gain a better understanding of the sintering performance of titanomagnetite. The main results obtained are as follows.

1. Ironsand had greater resistance to assimilation than traditional iron ores.
2. The relict ironsand particles in industrial sinter presented varied morphologies due to the spatial non-uniformity of sintering conditions. These can be well simulated by bench-scale sintering experiments, since the range of bench-scale experimental conditions employed in this study has been shown to produce relict ironsand morphologies consistent with the industrial sinter.
3. A relatively reducing atmosphere promoted the assimilation of ironsand into a liquid phase. The assimilation of ironsand during sintering in a reducing atmosphere started from the diffusion of calcium from the sinter blend into the lattice of the ironsand matrix. This in turn further decreased the melting point of titanomagnetite and accelerated the assimilation rate of ironsand particles. A reaction zone was formed near the boundary within ironsand particles where a perovskite phase was generated as a result of the reaction between TiO_2 and CaO.
4. When sintering at higher temperatures in a reducing atmosphere, ironsand particles underwent more assimilation. Along with the progress of assimilation, Ti in the perovskite phase was redistributed into glass and magnetite phases with the concentration in the former significantly higher than in the latter.
5. More Ti remained in original ironsand particles in a relatively oxidizing atmosphere, which was attributed to the high oxygen partial pressure suppressing the melting of SFCA and stabilizing TiO_2 in titanohematite.

REFERENCES

1. H. A. Cocker, J. L. Mauk, H. Rogers, A. B. Padya, and J. Ogiliev: *Proc. of the AusIMM New Zealand Branch 43rd Annual Conference*, AusIMM New Zealand Branch, Alexandra, 2010, pp. 165–74.
2. J.B. Wright: *N. Z. J. Geol. Geophys.*, 1964, vol. 7, pp. 424–44.
3. J.B. Wright and J.F. Lovering: *Mineral. Mag.*, 1965, vol. 35, pp. 604–21.
4. N.J. Bristow and C.E. Loo: *ISIJ Int.*, 1992, vol. 32, pp. 819–28.
5. I.F. Carmichael and J. Lowering: *Steel Times*, 1981, vol. 209, p. 416.
6. Y. Li, Y. Li, and R.J. Fruehan: *ISIJ Int.*, 2001, vol. 41, pp. 1417–22.
7. T. Paananen and K. Kinnunen: *Iron Ore Conference 2007*, AusIMM, 2007, pp. 361–67.
8. Z Yin, J Li, and S Yang: *Adv. Mater. Res.*, 2011, vols. 311–313, pp. 850–53.
9. I. C. Madsen and N. V. Y. Scarlett: in *Powder Diffraction: Theory and Practice*, R. E. Dinnebier and S. J. L. Billinge, eds., The Royal Society of Chemistry, Cambridge, U.K., 2008, pp. 298–331.
10. Bruker, TOPAS Version 4.2, Bruker AXS Inc., Madison, 2009.
11. M.I. Pownceby, C.M. MacRae, and N.C. Wilson: *International Heavy Minerals Conference*, AusIMM, Fremantle, 2001, pp. 69–74.
12. M.I. Pownceby, C.M. MacRae, and N.C. Wilson: *Mineral. Eng.*, 2007, vol. 20, pp. 444–51.
13. I. R. Harrowfield, C. M. MacRae, and N. C. Wilson: *Proc. of the 27th Annual MAS Meeting*, Microbeam Analysis Society, New York, 1993, pp. 547–8.
14. N.C. Wilson and C.M. MacRae: *Microsc. Microanal.*, 2005, vol. 11, pp. 434–35.
15. E. Park and O. Ostrovski: *ISIJ Int.*, 2003, vol. 43, pp. 1316–25.
16. G.T.R. Droop: *Mineral. Mag.*, 1987, vol. 51, pp. 431–35.
17. S.-M. Jung: *ISIJ Int.*, 2014, vol. 54, pp. 781–90.
18. M.B. Turner, S.J. Cronin, R.B. Stewart, M. Bebbington, and I.E.M. Smith: *Geology*, 2008, vol. 36, pp. 31–34.
19. J.B. Wright: *N. Z. J. Geol. Geophys.*, 1967, vol. 10, pp. 659–65.
20. F. Bosi, U. Halenius, and H. Skogby: *Am. Mineral.*, 2009, vol. 94, pp. 181–89.
21. B.A. Wechsler and C.T. Prewitt: *Am. Mineral.*, 1984, vol. 69, pp. 176–85.
22. R. Blake, R. Hessevick, T. Zoltai, and L. Finger: *Am. Mineral.*, 1966, vol. 51, pp. 123–29.
23. G.A. Lager, J.D. Jorgensen, and F.J. Rotella: *J. Appl. Phys.*, 1982, vol. 53, pp. 6751–56.
24. A.S. Brown, M.A. Spackman, and R.J. Hill: *Acta Crystallogr. A*, 1993, vol. 49, pp. 513–27.
25. A.K. Biswas: *Principles of Blast Furnace Ironmaking: Theory and Practice*, Cootha Publishing House, Brisbane, 1981, p. 194.
26. N.A.S. Webster, M.I. Pownceby, I.C. Madsen, and J.A. Kimpton: *ISIJ Int.*, 2013, vol. 53, pp. 774–81.
27. N.A.S. Webster, M.I. Pownceby, I.C. Madsen, A.J. Studer, J.R. Manuel, and J.A. Kimpton: *Metall. Mater. Trans. B*, 2014, vol. 45B, pp. 2097–105.
28. M. Binnewies and E. Milke: *Thermochemical Data of Elements and Compounds*, 2nd ed., Wiley, Weinheim, 2002.
29. K.C. Mills: *Slag Atlas*, 2nd ed., Stahleisen, Düsseldorf, 1995, pp. 131–37.